Preprint, 18th Conference on Numerical Weather Prediction
American Meteorological Society, Park City, UT

1B.4 Analysis and Prediction of 8 May 2003 Oklahoma City Tornadic Thunderstorm and Embedded Tornado using ARPS with Assimilation of WSR-88D Radar Data

Ming Hu[1] and Ming Xue[1,2]*

[1]Center for Analysis and Prediction of Storms, University of Oklahoma
[2]School of Meteorology, University of Oklahoma

1. Introduction

As a powerful tool in meteorological research and weather forecast, numerical simulation was used by many researchers in the past three decays to study the tornado and tornadogenesis. Trough 2-dimensional axisymemetric vortex models and three-dimensional asymmetric vortex models (Rotunno 1984; Lewellen 1993; Lewellen *et al.* 2000), the dynamics of the vortex flow near the tornado core were studied under the environment that guarantees tornado formation. To include the effect of tornado parent mesocyclone and study the tornado formation and evolution, different fully three-dimensional models with moist physics and turbulence were used by Grasso and Cotton (Grasso and Cotton 1995) and Wicker and Wilhelmson (Wicker and Wilhelmson 1995) to simulate tornado vortices produced in a storm that initializes from a warm bubble within a horizontally homogeneous environment based on the sounding derived from real tornadic storms. Besides unrealistic environment used in their study, the domain of the tornado-resolving grids are also limited by the computer source to only cover a small portion of the tornadic storms.

Other than computer source and nonhydrostatic model, the initiation of tornadic supercell and mesocyclone also plays a critical role in an effort to more accurately model tornadoes. As the only observational network that can resolve convective storms, the WSR-88D Doppler radar network of the United States provides a key information for storm-scale data assimilation and model initialization. Several advanced assimilation methods that can use radar observations to build up dynamically consistent storms in a model were developed, such as the four-dimensional variational (4DVAR) data assimilation method (Sun *et al.* 1991; Sun and Crook 1997,1998; Sun 2005) and the ensemble Kalman filter (EnKF) data assimilation, (Snyder and Zhang 2003; Wicker and Dowell 2004; Zhang *et al.* 2004; Tong and Xue 2005; Xue *et al.* 2006). Although both 4DVAR and EnKF demonstrate great advantages in the radar data assimilation for storms, their high computational cost hampers their application in the operation and with a large domain.

Another efficient way to assimilate multiple radar volume scans is to employ intermittent assimilation cycles with fast analysis methods, such as using ARPS (Advanced Regional Prediction System, Xue et al. 1995; 2000; 2001) three dimensional variational (3DVAR) analysis (Gao *et al.* 2002; 2004) to analyze the radar radial velocity data and other conventional data and the ARPS complex cloud analysis to retrieve thermodynamic and microphysical fields from the reflectivity according to semi-empirical rules (Zhang *et al.* 1998; Zhang 1999). This efficient intermittent assimilation system has been used with the WSR-88D data in several studies of tornadic thunderstorms at horizontal resolutions of 3 km (Xue *et al.* 2003; Hu and Xue 2006; Hu *et al.* 2006; Hu and Xue 2007) to initial tornado thunderstorms for the ARPS model.

For the 8 May 2003 case, the current ARPS model can capture well the propagation and general evolution of the tornadic thunderstorm up to 2 hours into forecast, using a 3-km horizontal resolution when starting from an initial condition into which radar data are properly assimilated. However, with a relatively coarse 3-km grid spacing, the forecasts miss many important details of the tornadic features, such as the hook echo and mesocyclone, which are indicative of the tornadic activities or potential. In this paper, experiments with 1-km, 100-m, and 50-m horizontal resolutions are conducted with the hope of being able to resolve more of the tornadic features or even the tornado itself.

This paper mainly discusses the results of the 1-km and 100-m experiments and the comparison of the tornado features captured by the two extra high resolution forecasts on the 100-m and 50-m grids. The detailed analysis of the 50-m forecast can be seen in our paper (Xue and Hu 2007). In

* Corresponding Author Address: Ming Xue, School of Meteorology, University of Oklahoma, NWC Suite 2500, 120 David Boren Blvd, Norman OK 73072 mxue@ou.edu

section 2, we introduce the case studied and the design of a set of 1-km experiments and one 100-m and one 50-m forecast. Section 3 analyzed the 1-km experiment results in detail and section 5 focuses on the 100-m forecast and its comparison with the 50-m forecast to demonstrate the prediction of the tornado. Results are then summarized and discussed in section 5.

2. Experimental Design

At about 2210 UTC (1610 Local Standard Time or LST) on 8 May 2003, Moore, a suburb city about 15 km south of the Oklahoma City, Oklahoma, was struck by a major tornado for the 4th time in 5 years. The tornado tracked east-northeast for about 30 km on the ground, from Moore to Choctaw, Oklahoma, and dissipated at 2238 UTC. This tornado caused large areas of F2-F4 (on Fujita scale of tornado intensity) damages and produced $370 million worth of damages and more than 100 injuries, but fortunately no death. It is named the OKC tornado by National Weather Service as it struck the general Oklahoma City area. Two additional short-lived tornadoes from the same storm were reported near Moore. The first brief tornado occurred at 2200 UTC. The second F0 tornado began at 2204 UTC and stayed on the ground and moved nearly 3 km in 6 minutes but dissipated just before the OKC tornado outbreak.The evolution of the tornado parent storm and the mesoscale and synoptic-scale settings in which the storm occurred are described in Hu and Xue (Hu and Xue 2007).

Similar to the 3-km experiments for the 8 May 2003 OKC tornadic thunderstorm case, the data from Oklahoma City WSR-88D radar (KTLX) are first preprocessed onto the 1-km grid and then used in data assimilation cycles. The low-level observations from the same radar are used to evaluate the results of assimilation and forecast.

All 1-km experiments are one-way nested within the 3-km control experiment described in the previous paper (Hu and Xue 2007). The horizontal domain of different grids are shown in *Fig. 1*. The 1-km grid is 280 km × 280 km in size and covers central and northern Oklahoma. The 100-m grid and 50-m grid are 160 km × 120 km and 80 km × 60 km in size, respectively, and are centered at the location of the OKC tornado. The same vertical grid is used in the 50-m, 100-m, 1-km grid, which is the grid stretched from 20 m at the surface to about 770 m at the model top that is located at about 21 km height.

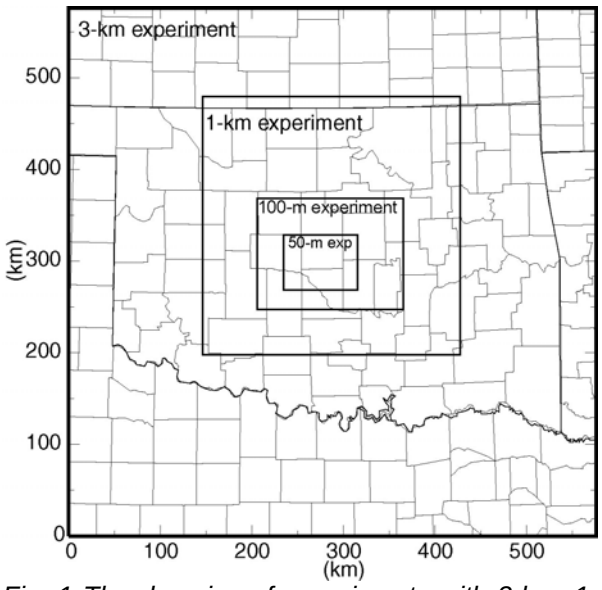

Fig. 1 The domains of experiments with 3-km, 1-km, 100-m, and 50-m horizontal grid spacing.

In 1-km control experiment, CNTL1km, radial velocity data are analyzed using the ARPS 3DVAR, while reflectivity data are used through the cloud analysis procedure. Five-min intermittent assimilation cycles are performed within a 70-min long assimilation window from 2030 to 2140 UTC. The temperature adjustment scheme based on the moist adiabatic temperature profile (MA scheme, Hu et al. 2006a) is used in the cloud analysis scheme. The mass divergence constraint is not imposed on the 3DVAR analysis of radial velocity except in the last 2 analysis cycles at 2135 and 2140 UTC in which a 2D divergence constraint is used with a weighting coefficient of 1000. Basically, the assimilation configurations of the 1-km control experiment are the same as those of 3-km experiment 5B30E30MA except for the use of the mass divergence constraint in the last 2 cycles and the 10-min longer assimilation window. To eliminate negative impacts of the storm south of the OKC tornadic thunderstorm (c.f.) on the assimilation, the reflectivity and radial velocity data associated with that storm are not included in the assimilation. Also, only reflectivity data exceeding 40 dBZ are used in the cloud analysis so as to avoid introducing weak cells that tend to grow spuriously in the model. Starting from the assimilation results, a 140-min forecast is made.

Three additional experiments are conducted, namely, Div2D1km, NoDiv1km, and CNTLZ1km. Experiment Div2D1km employs a 2D mass divergence constraint in all analysis cycles, while experiment NoDiv1km does not include the mass

divergence constraint at all. They are designed to study the impact of the mass divergence constraint on the storm structures in the forecast at a higher spatial resolution. Data denial experiment CNTLZ1km excludes the radial velocity data, and is intended to isolate the effects of such data. Otherwise, the settings of these experiments are the same as control experiment CNTL1km.

The OKC tornado was predicted by a one-hour high-resolution forecast on a 100-m horizontal grid that is one-way nested within the 1-km grid. The realistic initial condition interpolated from the 1-km assimilation result at 2140 UTC was used to start the 100-m forecast directly. To capture the fine structures of the tornado, a 50-m horizontal grid was further one-way nested within the 100-m run and finished 40 minutes of the forecast from an initial condition interpolated from the 20-minute forecast of the 100-m grid at 2200 UTC. Both 100-m and 50-m runs cover the entire period of the OKC tornado outbreak. The same full set of model physics is used in the three grids, except for turbulence, which use a full 3-D formulation in 100-m and 50-m grids but a vertical-only formulation in 1-km grid.

3. Experiment Results on 1-km Grid

3.1. Results of data assimilation

The analyzed radial velocity and reflectivity fields from CNTL1km, valid at 2135 UTC and mapped to the 1.45º elevation of the KTLX radar are plotted in *Fig. 2*, together with the corresponding 2136 UTC observations of the same radar.

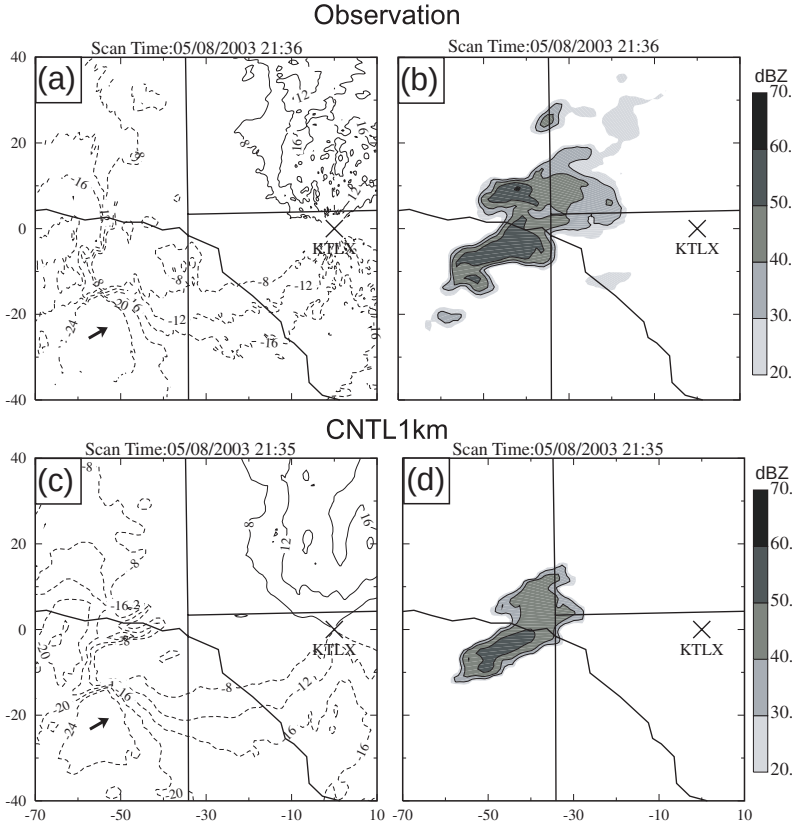

Fig. 2 The observed (a) radial velocity and (b) reflectivity fields at 2136 UTC from the KTLX radar at the 1.45º elevation and the corresponding (c) radial velocity and (d) reflectivity fields from the 2135 UTC CNTL1km analysis mapped to the same elevation. The x and y distances are in kilometer and are relative to the KTLX radar marked by '×'. Positive radial velocity values are contoured as solid lines from 8 to 24 m s^{-1} with 4 m s^{-1} intervals and negative as dashed lines from -24 to -8 m s^{-1} with the same intervals. The reflectivity values are plotted as shaded contours at 30, 40, 50, and 60 dBZ. The domain shown is 80 km on each side, representing to the portion of the1-km grid between 70 and 150 km in the east-west direction and from 50 to 130 km in the north-south direction. The short arrows in radial velocity panels show the direction of radial velocities near their peak value.

At 2136 UTC, the southwestern end of the observed OKC storm showed a hook-shaped echo that was colocated with a strong cyclonic vortex center, as indicated by a strong radial velocity gradient at about (-54 km, -18 km) (*Fig. 2*a, b). Also, a strong left-moving split cell existed due north of the main OKC storm.

The 2135 UTC analysis of CNTL1km correctly captures the main OKC storm, but misses the hook-shaped echo and the core of the left-moving cell (*Fig. 2*d). The use of only reflectivity data exceeding 40 dBZ is part of the reason for missing weaker features and smaller-scale structure; the smoothing to the hydrometeor fields in the cloud analysis is another contributor. On the other hand, the analyzed radial velocity field closely replicates the pattern and intensity of the observed cyclonic vortex center and the environmental winds (*Fig. 2*c).

The analyzed radial velocity fields at 2135 UTC from experiments CNTLZ1km, Div2D1km, and NoDiv1km are plotted in *Fig. 3*. The analyzed reflectivity fields of these experiments are the same as that in *Fig. 2*d because the same data and cloud analysis procedure are used.

The analyzed radial velocity fields of Div2D1km and NoDiv1km also show similar patterns of the cyclonic rotation center and of the environmental winds as the observed ones despite the difference in the use of the mass divergence constraint (*Fig. 3*b, c). When the radial velocity data are not used, as in CNTLZ1km, the analyzed radial velocity field is much smoother and loses the cyclonic vortex center at the southwestern end of the OKC storm entirely (*Fig. 3*a). The environmental flow pattern also deviates from the observations more, at this and other levels (latter not shown).

Clearly, the analysis of radial velocity via the 3DVAR is able to provide detailed flow structures on the 1-km grid.

3.2. Results of forecasting

3.2.1. Evolution of maximum surface vertical vorticity

To examine the evolution of low-level rotation, the time series of the predicted maximum vertical vorticity at the surface in the OKC storm are plotted (*Fig. 4*) for the first hour of forecast for experiments CNTL1km, CNTLZ1km, Div2D1km, and NoDiv1km.

For three experiments that assimilate radial velocity data, the evolution of the maximum surface vorticity shows different characteristics before and after 2205 UTC. During the first period

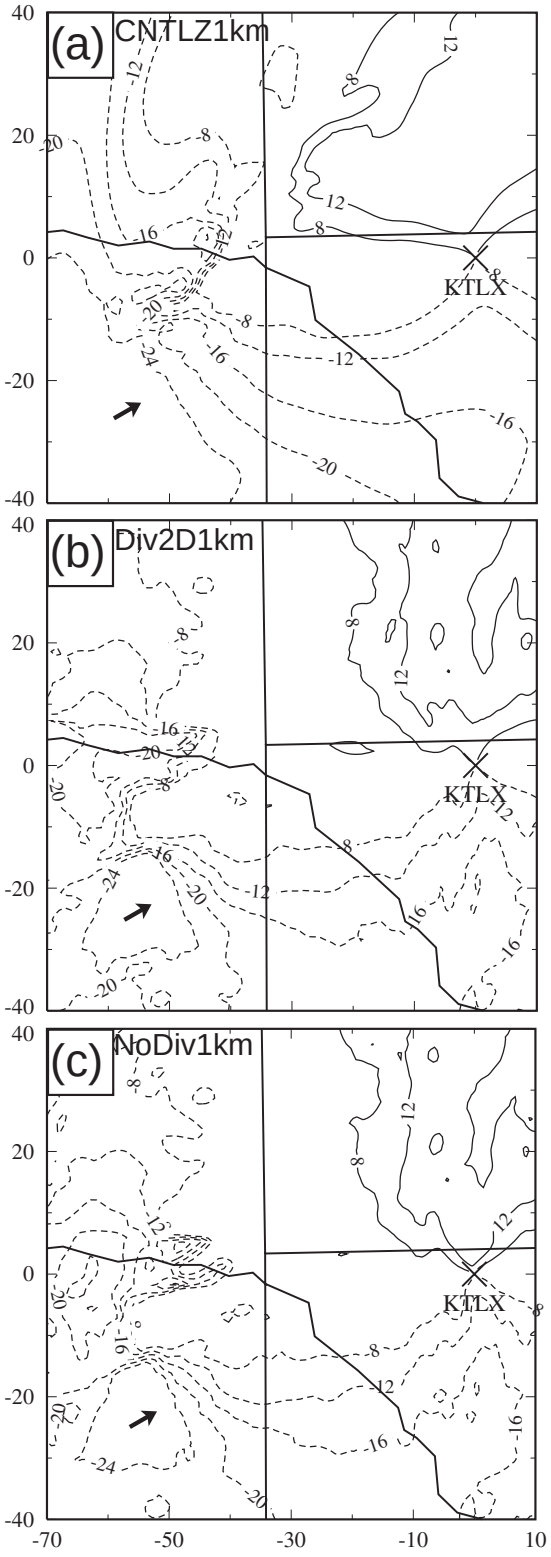

Fig. 3 As in Fig. 2c, but for experiments (a) CNTLZ1km, (b) Div2D1km, and (c) NoDiv1km.

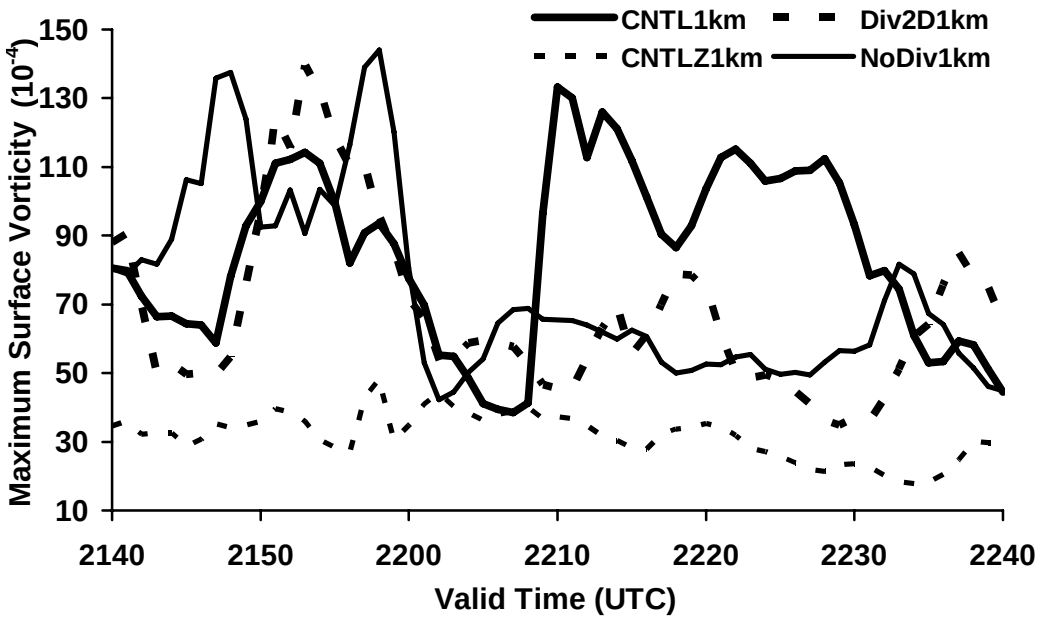

Fig. 4 Maximum surface vertical vorticity in the predicted OKC tornadic thunderstorm during the first hour of forecast for experiments CNTL1km, CNTLZ1km, Div2D1km, and NoDiv1km.

that is before 2205 UTC, the maximum surface vorticity exhibits large oscillations between 0.006 and 0.014 s^{-1} in all three experiments. During the second period from 2205 to 2240 UTC, which covers the OKC tornado outbreak, the maximum surface vorticity in CNTL1km rapidly increases to a high value of 0.013 s^{-1} within about 5 minutes and remains above 0.009 s^{-1} for approximately 20 minutes, while those of Div2D1km and NoDiv1km remain mostly below 0.006 s^{-1}. An examination of the surface vorticity fields of CNTL1km shows that the maximum values between 2148 and 2155 UTC correspond to one vorticity center while those between 2110 and 2130 UTC correspond to another.

For experiment CNTLZ1km, in which radial velocity data are not analyzed, the maximum surface vorticity is always much lower than those of the other three experiments, indicating the important impact of the radial velocity analysis on the formation of strong low-level vorticity centers.

Guided by the above analysis of the maximum surface vorticity, we discuss the forecast fields in the first and second periods, respectively.

3.2.2. Forecast in the first period

The predicted radial velocity and reflectivity fields at 10 minutes into the forecast from CNTL1km, CNTLZ1km, Div2D1km, and NoDiv1km are shown in *Fig. 5*. As before, the fields are mapped to the 1.45º elevation of the KTLX radar, and the corresponding observed fields at 2151 UTC are also plotted.

In 15 min from 2136 to 2151 UTC, the observed OKC storm propagated east-northeastward by about 10 km (*Fig. 2*a and b, *Fig. 5*a and b) and still had a weak hook-shaped echo at its southwestern end and a strong left-moving split cell to its north (*Fig. 5*b). The low-level cyclonic rotation at its southwestern end became weaker in this 15 min but was identifiable, with its center located at (-42 km, -10 km) (*Fig. 5*b).

At 2150 UTC, the 10-minute forecast of CNTL1km captures well the main part of the OKC storm in terms of the reflectivity pattern (*Fig. 5*d). A sharp hook-shaped echo is found at the southwestern end of the predicted storm and a left-moving cell is present in the prediction, but is attached to instead of being separate from the main cell. The low-level cyclonic rotation is also evident (*Fig. 5*c), showing as a clear cyclonic radial velocity couplet near (-40 km, -5 km). The rotation actually appears stronger in the forecast than in the observation.

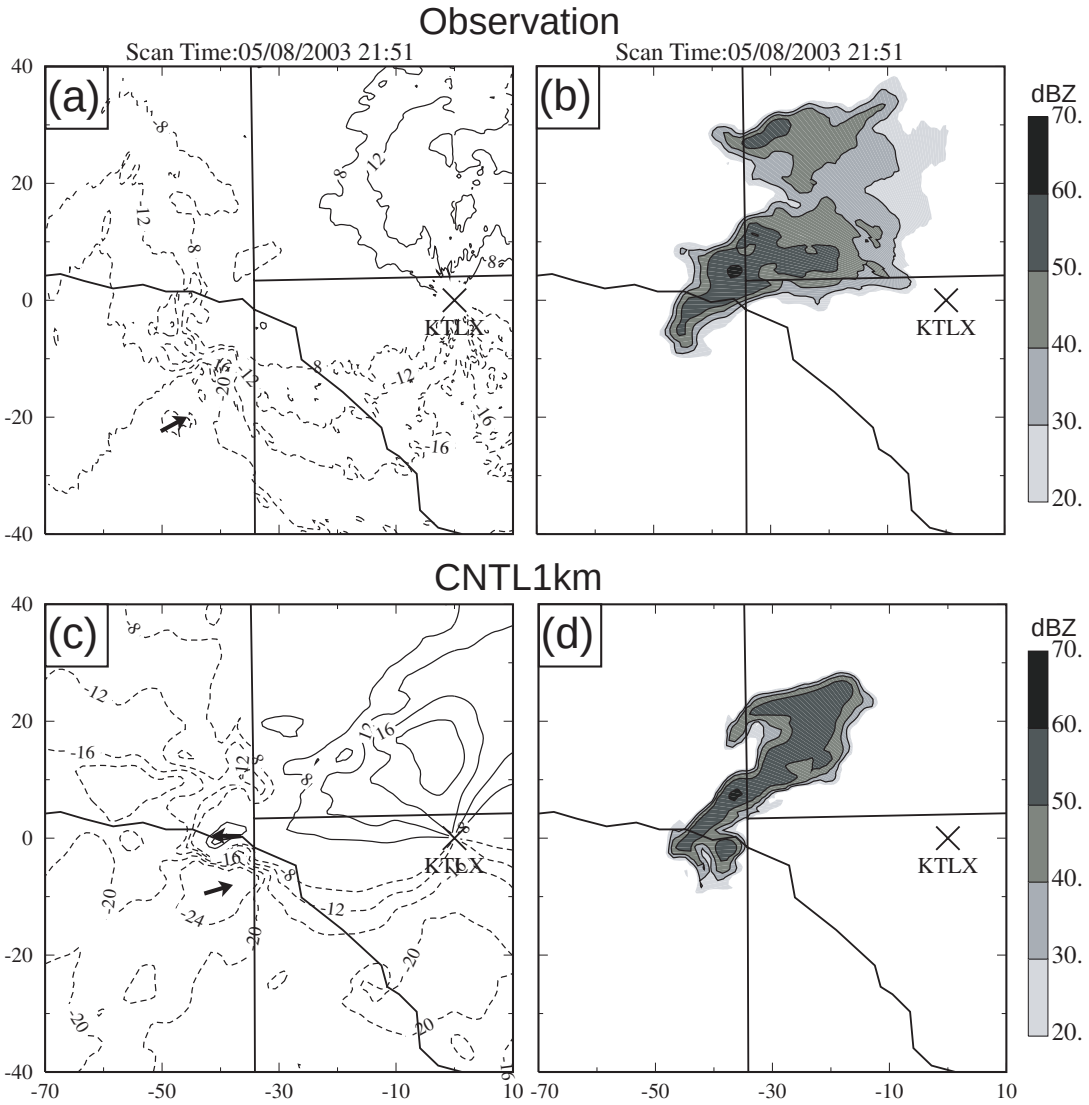

Fig. 5 As in Fig. 2, but for (a) and(b) observations at 2151 UTC and 10-minute forecast of experiments (c) and (d) CNTL1km, (e) and (f) CNTLZ1km, (g) and (h) Div2D1km, and (i) and (j) NoDiv1km.

Without the radial velocity assimilated, experiment CNTLZ1km overpredicts the propagation of the main storm during the same period, and misses the cyclonic rotation at the southwestern end (*Fig. 5*e, f). Instead, a small anticyclonic feature centered at around (-35 km, 0 km) is identifiable in both reflectivity and radial velocity fields. The left-moving cell is completely missing.

Div2D1km and NoDiv1km differ from CNTL1km only in the use of the mass divergence constraints. Their forecasts are similar to that of CNTL1km but with some small differences (*Fig. 5*g-j). The hook-shaped echo of the main storm is not captured by Div2D1km (*Fig. 5*h). A cyclonic radial velocity couplet is captured in the forecasts of both Div2D1km and NoDiv1km, as is in CNTL1km, but the radial velocity field of the former is much smoother because of the use of a 2D mass divergence constraint, while that of the latter is much noisier because of the absence of any mass divergence constraint (*Fig. 5*c, g, i).

The above analysis indicates that the initial low-level cyclonic rotation analyzed using the 3DVAR with radial velocity data is spun up during the first 20 minutes of forecast on the 1 km grid. The use of radial velocity data in the assimilation noticeably improves the quality of the short-term forecast for the main storm in terms of both wind and reflectivity fields.

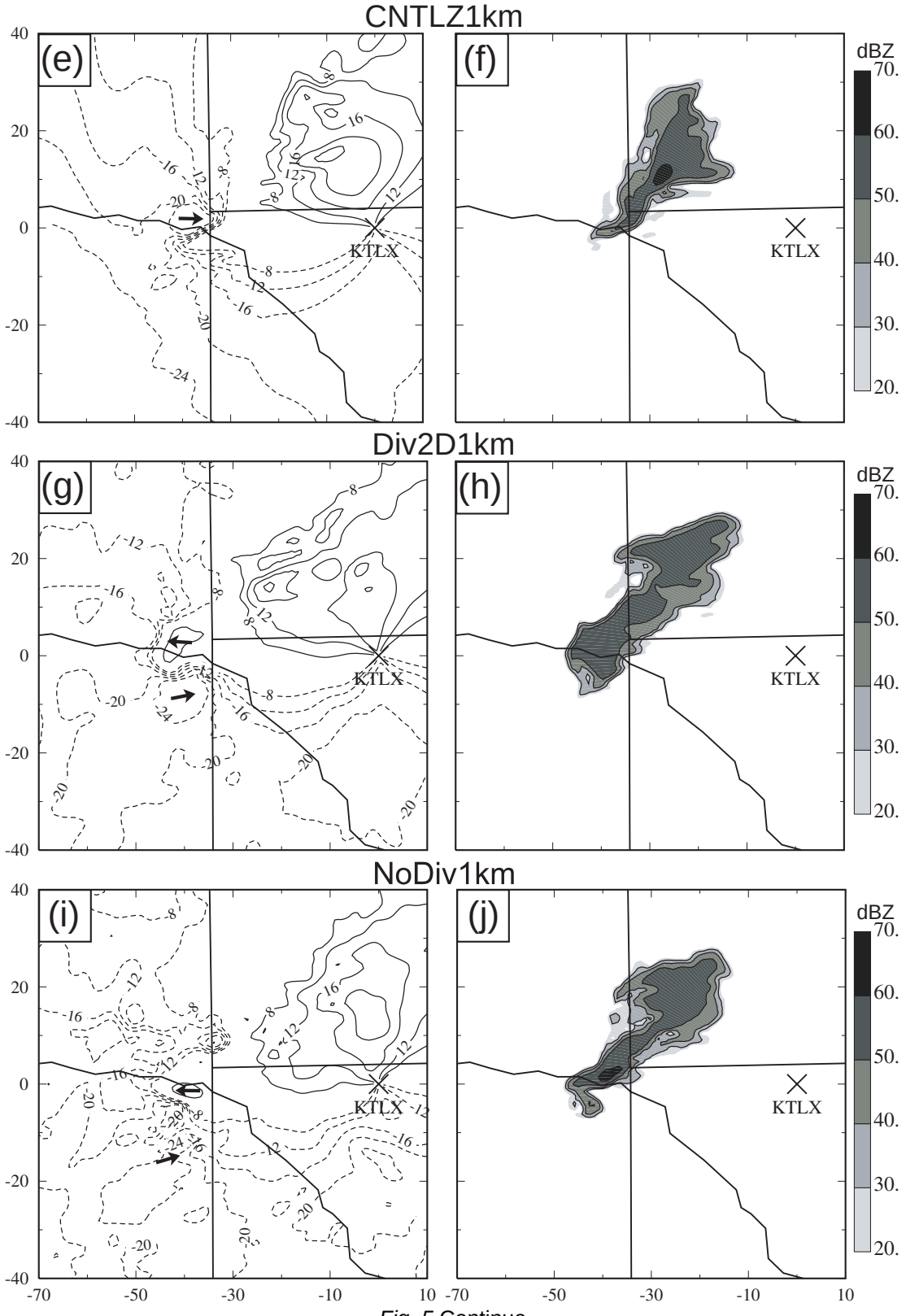

Fig. 5 Continue

3.2.3. Forecast in the second period

The maximum surface vertical vorticity in CNTL1km shows large values from 2210 to 2230 UTC which partially coincide with the occurrence of the tornado from 2210 to 2238 UTC of that day. To evaluate the forecast in terms of the tornadic features such as mesocyclone and hook echo, the observed reflectivity fields at the 1.45º elevation of the KTLX radar (left column) and the corresponding predicted reflectivity fields from CNTL1km (right column) are plotted in *Fig. 6*, at 10-min intervals from 2210 to 2230 UTC. The corresponding radial velocity fields are plotted in *Fig. 7*.

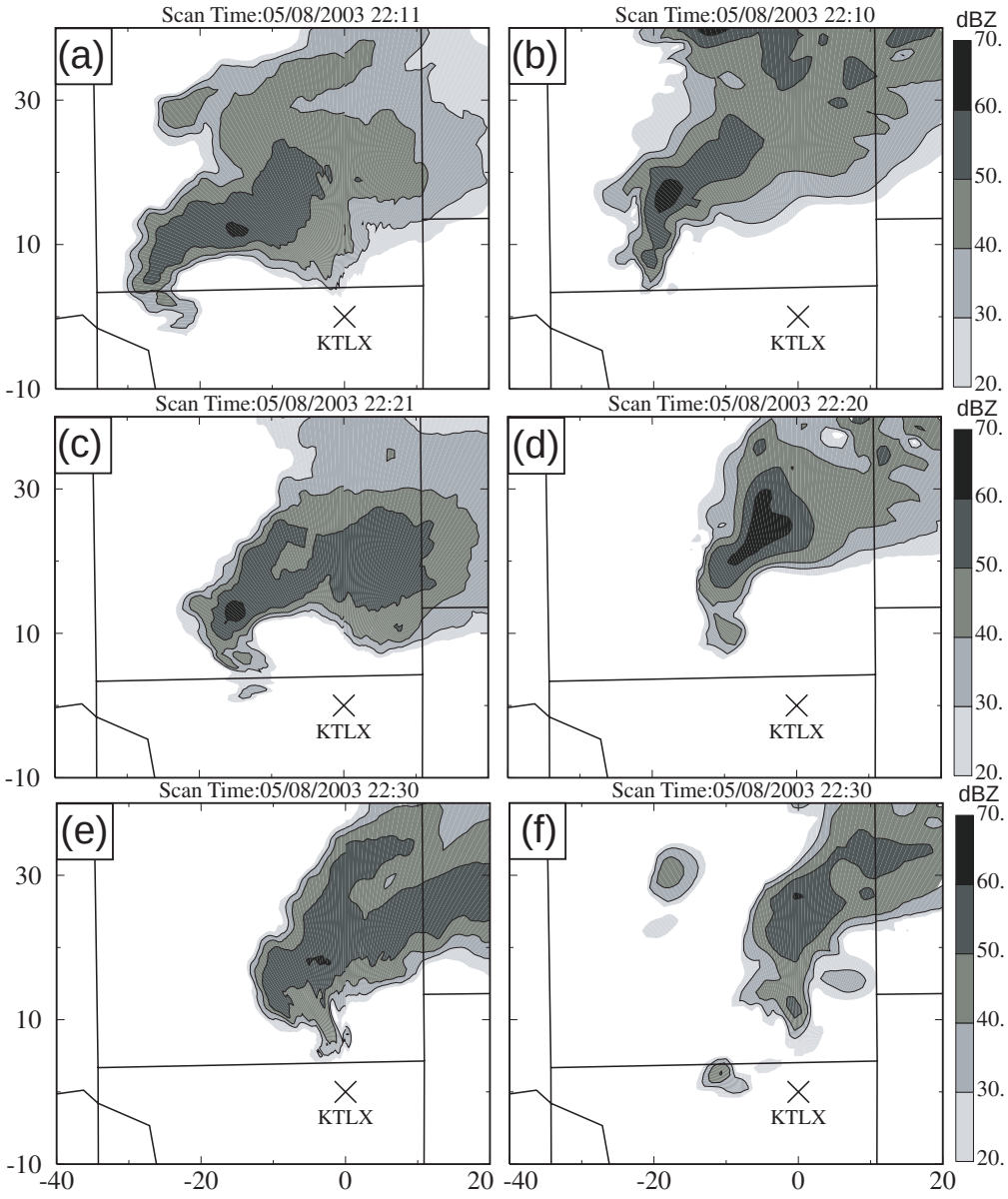

Fig. 6 (a), (c), and (e) the observed reflectivity fields at the 1.45º elevation of the KTLX radar, and (b), (d), and (f) the predicted reflectivity fields at the same elevation from experiment CNTL1km, at 10-minute intervals from 2210 to 2230 UTC 8 May 2003. The x and y distances are in kilometer and are relative to the KTLX radar marked by X. The reflectivity contours are at 30, 40, 50, and 60 dBZ. The domain shown is 60 km by 50 km, representing the portion of the 1-km grid between 102 and 162 km in the east-west direction and from 80 to 130 km in the north-south direction.

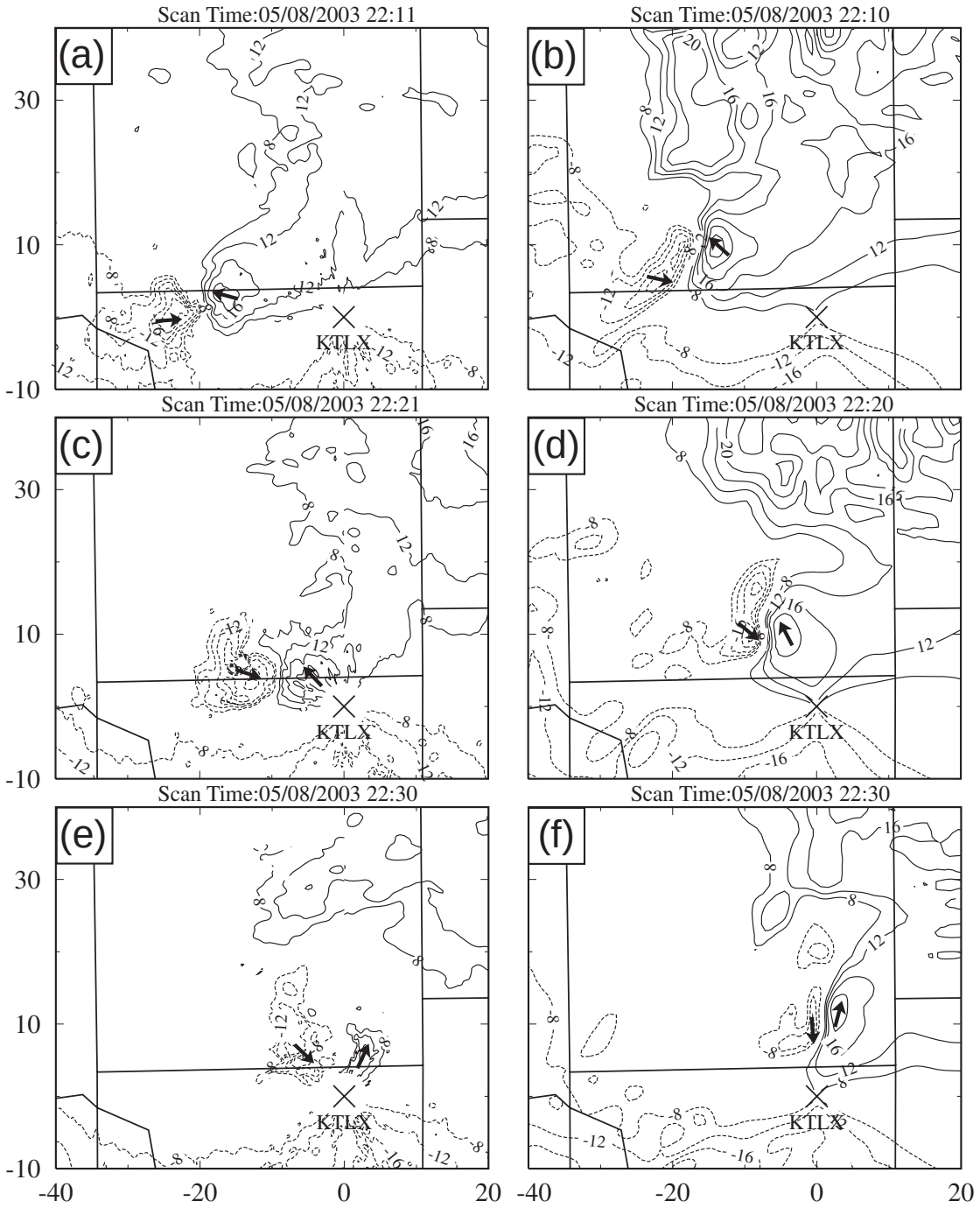

Fig. 7 (a), (c), and (e) the observed radial velocity fields at the 1.45º elevation of the KTLX radar and (b), (d), and (f) the predicted radial velocity fields at the same elevation from experiment CNTL1km, at the same time as Fig. 6. The domain and x and y coordinates are also same as Fig. 6. The positive radial velocity is contoured as solid lines from 8 m s^{-1} to 24 m s^{-1} with 4 m s^{-1} intervals and negative as dashed lines from -8 m s^{-1} -24 m s^{-1} with the same intervals. The short arrows show the direction of radial velocity in their maximum value area.

The observed reflectivity field of the OKC storm at 2211 UTC showed a hook echo at its southwestern end (*Fig. 6*a), indicating the presence of a tornadic circulation. In the next 20 minutes, the main OKC storm propagated east-northeastward, maintaining the, although weaker, the hook echo (*Fig. 6*c, e). The forecast of the main OKC storm propagates in the similar direction and speed as the observed one did but with about 10-km northeastward displacement error throughout the period. The most interesting feature of the predicted storm is that it also develops and maintains a hook echo at its southwestern end (*Fig. 6*b, d, f), although the hook is not as sharply defined as in the observations.

To decide if vortices can be classified as mesocyclone, the criteria that radial velocity difference across the cyclonic couplet is large than 30 m s^{-1} and lasts at least 5 minutes is used (Trapp *et al.* 2005). Based on this criteria, a mesocyclone was found in the radial velocity observations from 2211 to 2230 UTC and was also colocated with the observed hook echo (*Fig. 7*a c e, *Fig. 6*a, c, e). During this 20 minutes, the mesocyclone moved mainly eastward, approaching the KTLX radar with a slight northward component, and became weaker and less organized. However, the damage survey of the OKC tornado indicates that the tornado became stronger during these 20 minutes. One possible reason for this discrepancy is that when the mesocyclone approached the KTLX radar from the 25 to 5 km in radial range, the height of the observed mesocyclone at the 1.45° elevation decreased from 630 m to 127 m. The mesocyclone became weaker and less organized in near surface level because of fraction and turbulence.

The forecast of CNTL1km for the above period gives a mesocyclone that is even stronger than the observed one and also colocated with the predicted hook echo (*Fig. 7*, *Fig. 6*b, c, d). The predicted mesocyclone propagates mostly eastward at a similar speed as the observed one but with about 10 km northeast location errors; it remains strong and well-defined up to 2220 UTC and becomes weaker afterwards. In the predicted radial velocity fields, large unobserved perturbations exist in the northeastern part of the plotting domain. These perturbations are associated with the split left-moving cells in the model that split later and evolve slower than the observation; the observed left mover was out of the plotting domain at these times.

The above analysis shows that the mesocyclone associated with the OKC tornado is captured by CNTL1km at the right time and about the right place. To further study the vertical structure of this mesocyclone, vertical vorticity and wind fields at the surface, 1 km, 2 km, and 3 km MSL from the 35-minute forecast are plotted in *Fig. 8*. At the surface, a strong isolated vorticity center with a maximum value of 0.011 s^{-1} is located at the area of the emsocyclone discussed earlier (*Fig. 8*a and *Fig. 7*). Immediately northeast of the vorticity center is a strong surface convergence center, indicating the presence of a strong updraft adjacent to the vorticity center. At 1 km and 2 km MSL, strong vorticity centers with maximum values of over 0.02 s^{-1} are located right above the surface one. At 3 km MSL, the vorticity center is still strong with a maximum value of 0.025 s^{-1} but is located slightly north of the low-level ones. Clearly, the predicted mesocyclone extends through the lower levels of atmosphere and suggests a high possibility of tornadogenesis but the 1-km grid spacing is too coarse to resolve the tornado itself.

To analyze the results of the other three experiments, the predicted radial velocity and reflectivity fields at the 1.45º elevation from the 40-minute forecasts (valid at 2220 UTC) of Div2D1km, NoDiv1km, and CNTLZ1km are plotted in *Fig. 9*.

In CNTL1km, the 2D mass divergence constraint is imposed on the last two 3DVAR radial velocity analyses only to help organize the analyzed circulations. In Div2D1km, the same constraint is imposed on all analysis cycles. At 2220 UTC, the OKC tornado was in its mature stage, the 40-min prediction of Div2D1km has a strong mesocyclone but only shows a weak hook echo at the southwestern end of the main storm (*Fig. 9*a, b, *Fig. 6*d, and *Fig. 7*d). Both emsocyclone and weak hook echo are located 20 km north of the observed one, which is much larger than the location error of CNTL1km forecast at this time. On the other hand, when no mass divergence constraint is used in the analysis cycles, as in NoDiv1km, the predicted mesocyclone circulation and hook echo are not as strong and well-defined compared to CNTL1km (*Fig. 9*c, d, *Fig. 6*d, *Fig. 7*d). Therefore, the mass divergence constraint needs to be used carefully because it apparently has a noticeably impact on the detailed structures of the predicted storms.

Although the above experiments with different mass divergence constraint for radial velocity analysis result in different detailed storm structures, they all predict, more or less, the

mesocyclone. When radial velocity data are not used in experiment CNTLZ1km, no hook echo or cyclonic circulation is found in the prediction at 2220 UTC (*Fig. 9*e, f) or other time (not shown). The large differences found between the forecasts with and without radial velocity data indicate that the radial velocity analyses with the radar data that has captured cyclonic rotations are critical in building up the cyclonic rotation in the initial conditions, which affect significantly the subsequent forecast

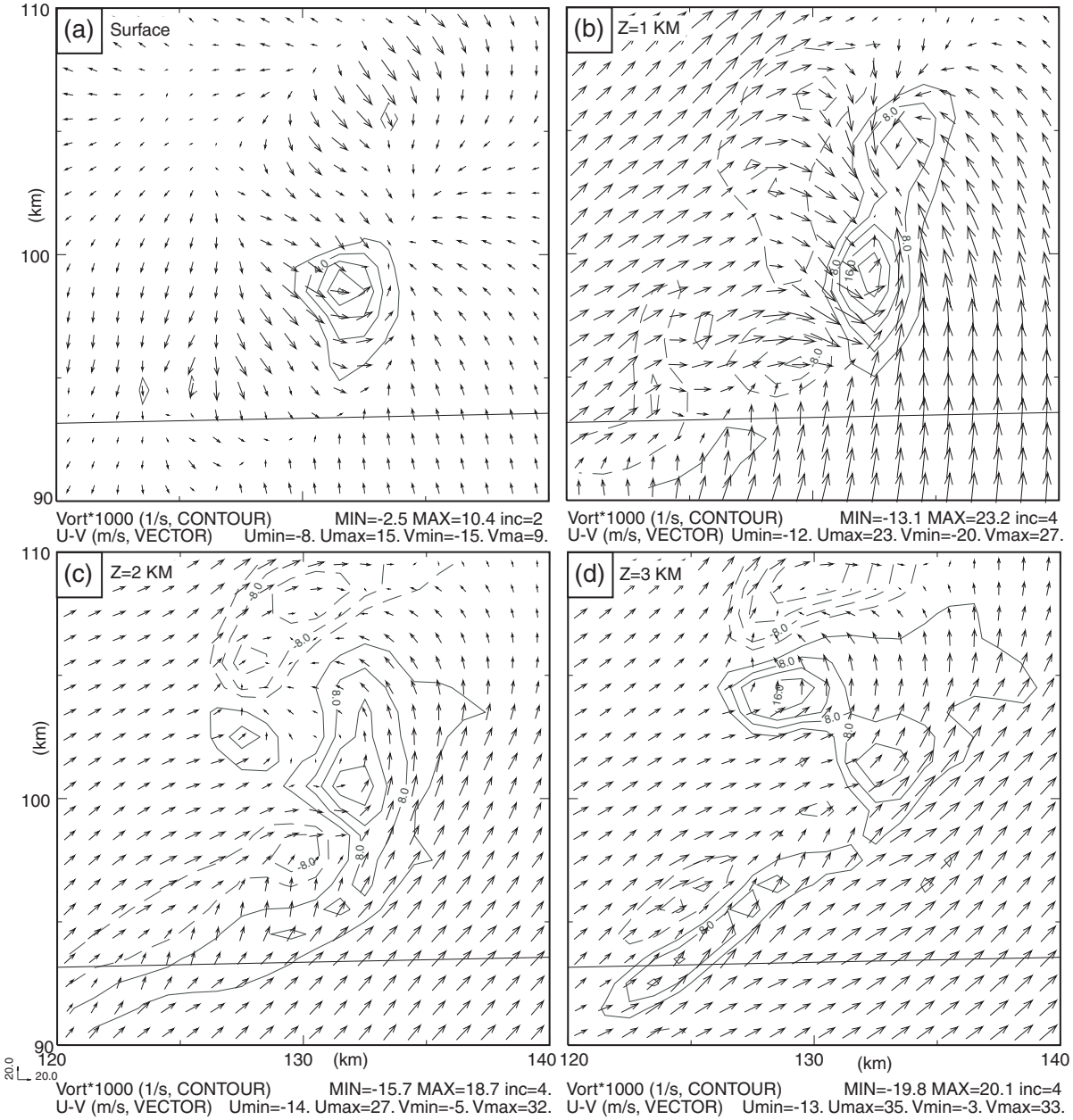

Fig. 8 Predicted vertical vorticity and wind fields at the (a) surface, (b) 1 km, (c) 2 km, and (d) 3 km MSL from the 40-minute forecast (valid at 2220 UTC) of experiment CNTL1km. The domain shown is 20 km by 20 km, representing the portion of the 1-km grid between 120 and 140 km in the east-west direction and from 90 to 110 km in the north-south direction.

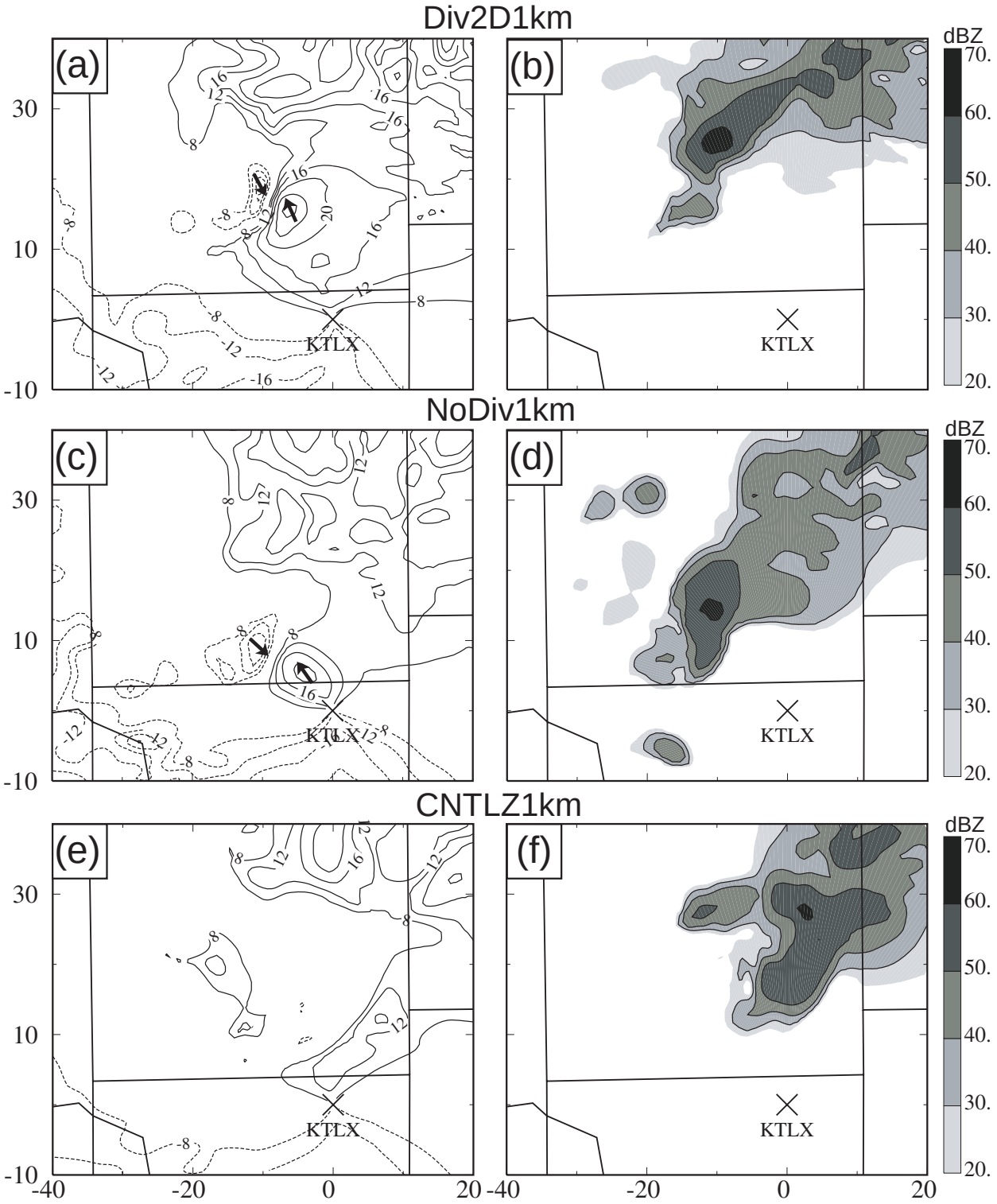

Fig. 9 Left column as in Fig. 7d and right column as in Fig. 6d, but for experiments (a) and (b) Div2D1km, (c) and (d) NoDiv1km, and (e) and (f) CNTLZ1km.

4. Forecast on Tornado-resolving Grid

In this paper, we mainly discuss the forecast on the 100-m grid and the comparison of the forecasts on the 50-m and 100-m grids. The detailed discussion on the 50-m grid forecast can be found in Xue and Hu (2007). The goal of the experiment with extra-high resolution is to capture the OKC tornado itself, instead of just the parent mesocyclone when a coarse resolution is used.

4.1. The evolution of predicted tornadoes

Several tornadic indicators are combined to determine the existence of the tornado in the forecast. The time series of the maximum surface vertical vorticity, maximum surface wind speed, and minimum perturbed surface pressure from both 100-m grid and 50-m grid forecasts are plotted in *Fig. 10*. The 100-m grid shows clear features of tornado outbreak in 30 to 46 min of the forecast valid from 2210 to 2226 UTC, during which a rapid drop of the minimum surface pressure concurs with a quickly increase in the maximum surface vertical vorticity and surface wind speed. An examination of the surface fields shows that all these extremes are associated with a small region of strong low-level circulation (not shown) during this 16-min forecast except for a short break marked by a sharp notch in the maximum surface vertical vorticity and the maximum surface wind speed and a bulge in the minimum surface pressure at about 2215 UTC. The life span of the first tornado when its intensity is F1 (32-50 m s^{-1} in the Fujita scale) according to the maximum surface wind and above is 4 minutes, from 2211 to 2215 UTC and the second one is 11 minutes from 2215 to 2226 UTC. In fact, the second tornado reaches the intensity of F2 (50-70 m s^{-1}) during 2217 to 2221 UTC with the peak maximum surface wind speed of 58.8 m s^{-1}, peak maximum surface vorticity of 0.57 s^{-1}, and maximum surface pressure deficit of -33.0 hPa. Clearly, the intensity and time span of these predicted circulations on the 100-m grid, in terms of the above measures, qualify them as actual tornadoes.

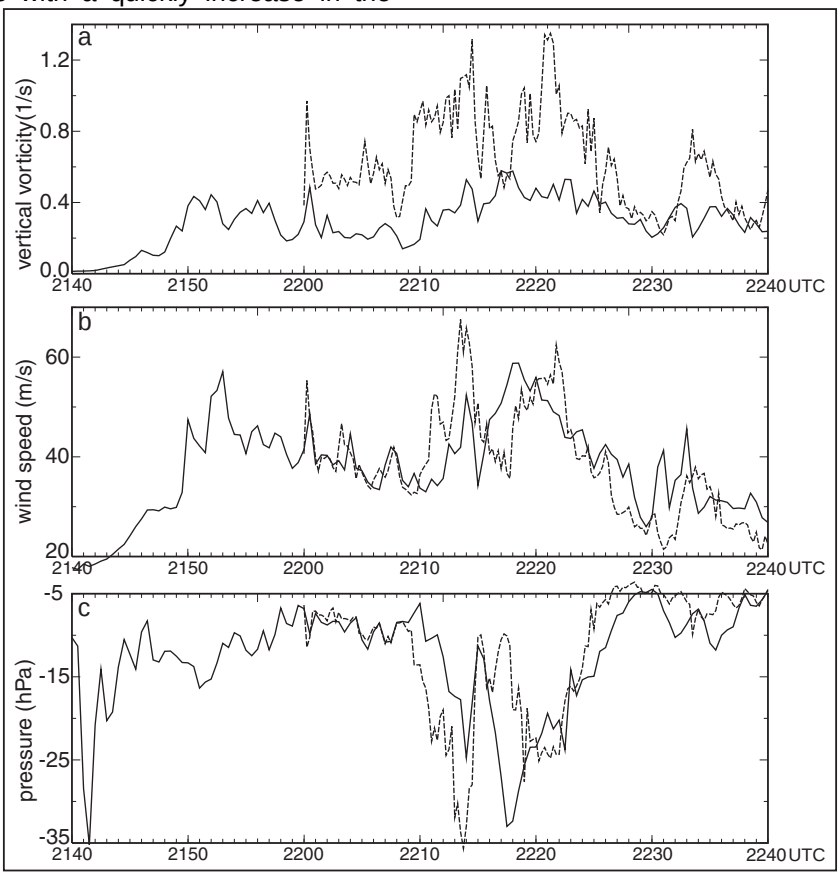

Fig. 10 The time series of (a) maximum surface vertical vorticity, (b) maximum surface wind speed, and (c) minimum perturbed surface pressure of the 60-min forecast starting from 2140 UTC on the 100-m grid (solid line) and the 40-min forecast starting from 2200 UTC on the 50-m grid (dashed line, borrowed from Xue and Hu (2007)).

When compare the evolutions of the same extreme between the 50-m and 100-m grids, they fit with each other in terms of evolution trend but has big difference in terms of intensity. Almost during the same time period from 2210 to 2225 UTC, which is over-laid with the real tornado outbreak from 2210 to 2238 UTC, both the 50-m and 100-m grids produce two tornadoes marked by the rapid drop of minimum surface pressure and the quick increase of maximum surface wind and vertical vorticity. When the finer grid spacing used, the intensity of vertical vorticity is increased significantly. The maximum surface vertical vorticity almost doubles in the 50-m forecast than in the 100-m forecast during the entire tornado outbreak. While the maximum surface wind speed and the pressure deficit are not so sensitive to the grid spacing, the peak value of these two variables are only significant higher in the 50-m forecast during a short period in the first predicted tornado outbreak.

The first 20 min forecast on the 100-m grid also gives a brief tornado at around 2152 UTC. This was also happened for the real tornadic thunderstorms. Right before the OKC tornado, there are two weak tornadoes produced from the same thunderstorm but at 10 min later. Also the minimum surface perturbed pressure shows a big drop during the first 2 min of the forecast on the 100-m grid (*Fig. 10*c) but this pressure drop is due to the pressure oscillation in the entire forecast domain instead of inside a strong circulation and reflects the adjustment during the initial period of the forecast starting from the field interpolated from the 1-km assimilation.

The modeled tornado paths represented by the circulation center of the predicted tornadoes on the 50-m grid and 100-m grid are plotted in *Fig. 11* along with the observed tornado damage path to study the location of tornado outbreak captured by model. Unlike the real OKC tornado that caused a 30 km long F2 to F4 damage path in the southern Oklahoma City area, the predicted path on the 100-m grid is about 15 km long with a short break at 2215 UTC and is located in the central area of the Oklahoma City, about 8 km north of the observed path, while the predicted tornadoes on the 50-m grid pass the same area during the same period as the 100-m grid ones but the second one lasts much shorter in time and path than its 100-m counterpart.

The predicted reflectivity at the surface of the 100-m forecast valid from 2210 to 2220 UTC is plotted in *Fig. 12* with 5 min intervals, together with the nearest observed reflectivity at the 1.45° elevation of the KTLX radar. This was the first 10 min of the OKC tornado life cycle and a sharp hook echo was appended at the southwest end of supercell (*Fig. 12*b, d, and f). At the same time, the similar hook echo is shown at the same position as the observed one relative to their parent supercell on the 100-m forecast (*Fig. 12*a, c, and e). The main body of the predicted supercell has a northwest location error of about 10 km. Comparing to the same time forecast on the 1-km grid, the 100-m not only captures many fine structures of the hook echo but also improves the location forecast of the parent supercell (*Fig. 6*b, d).

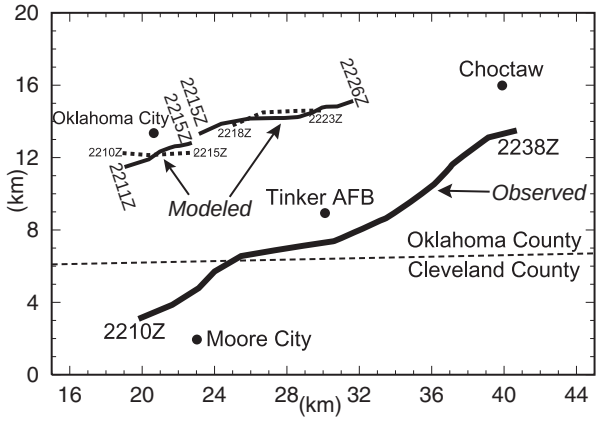

Fig. 11 The observed damage path of the 8 May OKC tornado and the path of the modeled tornado on 100-m grid (solid line) and 50-m grid (dashed line, borrowed from Xue and Hu (2007)) represented by the central location of the tornado circulation. The life span of each tornado is also indicated by the time at the beginning and end of the path. The domain shown is 30 km × 20 km in size, representing the portion of the 50-m grid between 15 and 45 km in the east-west direction and from 0 to 20 km in the north-south direction.

4.2. Detailed structure of predicted tornadoes

To study the fine structures of the predicted tornado, we zoom in a 2 km × 2 km domain that covers immediate area of the predicted tornado. The surface wind, surface vertical vorticity, and perturbed surface pressure fields in these small domains are plotted in the right column of *Fig. 13* for the forecast of the 100-m grid valid at 2214, 2217.5, and 2220 UTC, respectively, with gust fronts indicated by frontal symbols. The left column of *Fig. 13* is the forecast of the 100-m grid at the same time and within the same horizontal

small domain as the right column of the figure,*Fig. 13* but for the X-Z cross-section of the vertical velocity and vertical vorticity along the line indicated in the corresponding right panel.

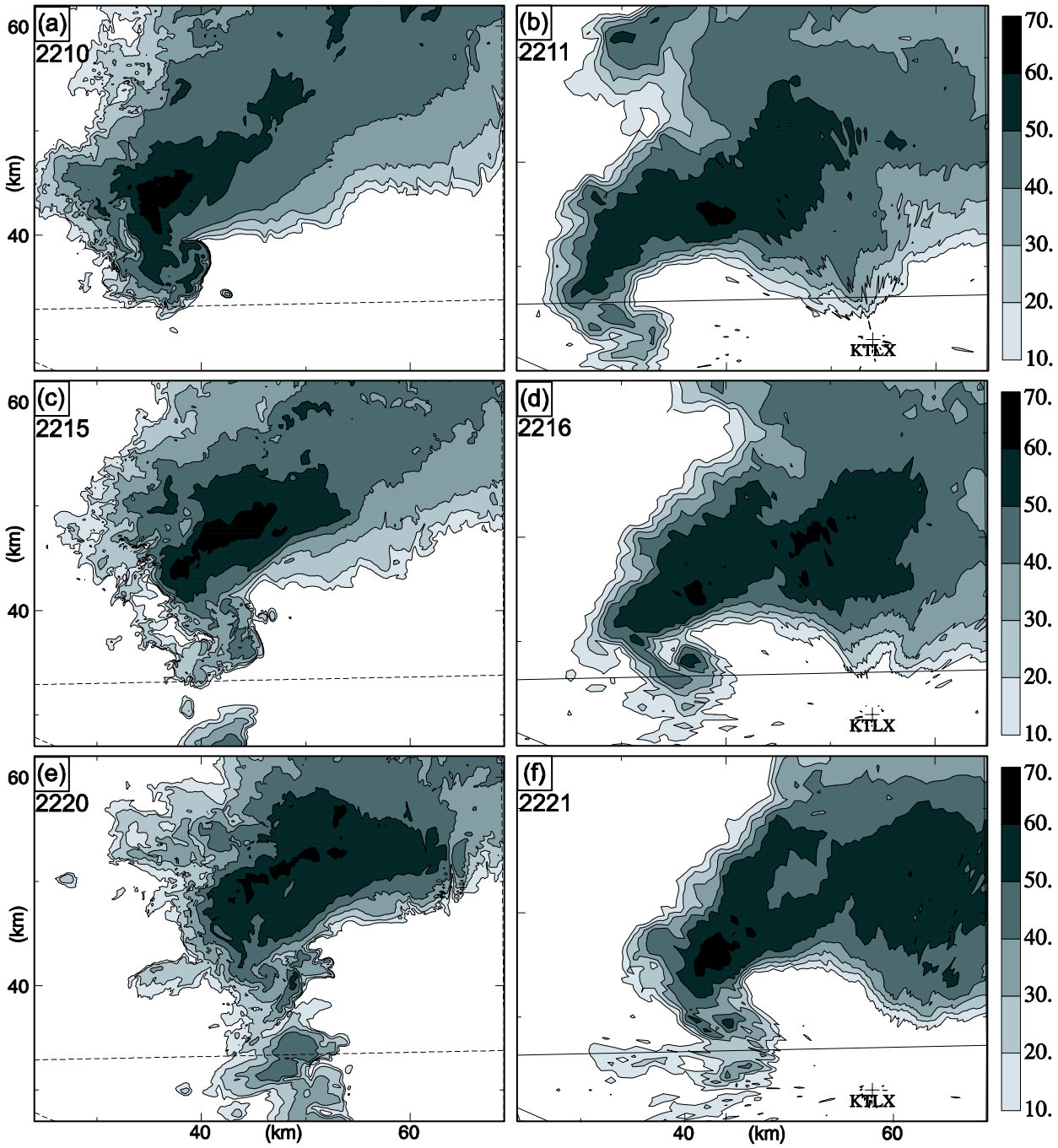

Fig. 12 (a), (c), and (e) Predicted reflectivity field at the surface in 30 to 40 min of the 100-m forecast with 5 min intervals and (b), (d), and (f) observed reflectivity at the 1.45° elevation of the KTLX observation at 2211, 2216, and 2221 UTC. The domain shown is 45 km × 35 km in size, representing the portion of the 100-m grid between 47 and 92 km in the east-west direction and from 30 to 65 km in the north-south direction.

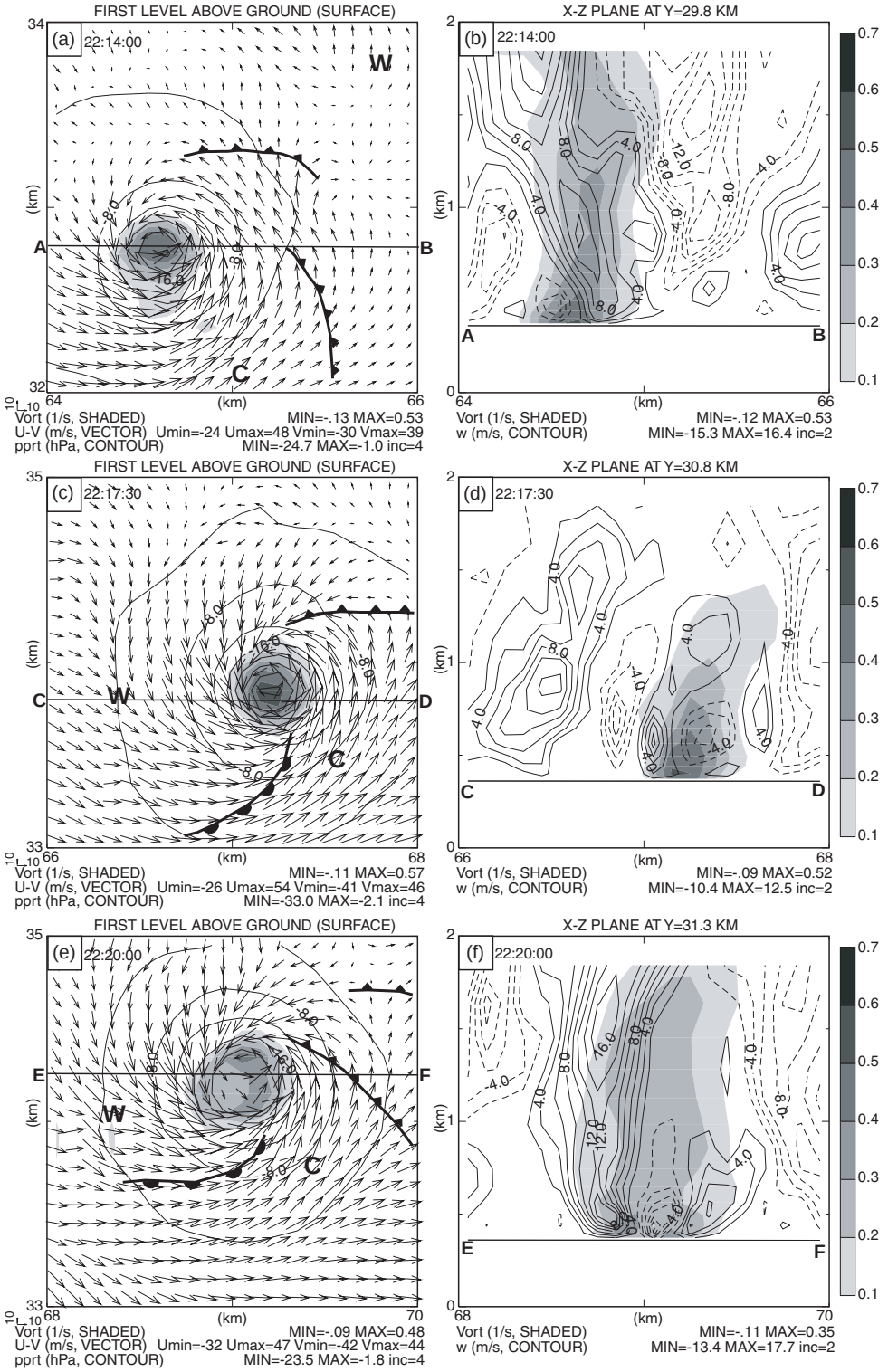

Fig. 13 (a) (c), and (e) Predicted vertical vorticity (shaded), wind (vector), perturbed pressure (contour) fields at the surface from the 34, 37.5, and 40 minutes of forecast of the 100-m grid (valid at 2214, 2217.5, and 2220 UTC) together with the location of gust front (frontal symbol) and the warm (W sign) and cold (C sign) center, and (b) (d), and (f) Y-Z cross section of vertical vorticity (shaded) and vertical velocity (contour) at the same time along the line shown in (a), (c), and (e), respectively. The domain is 2 km by 2 km and covers area indicated by the coordinate number in the corner. The numbers below the panels are the maximum and minimum values of the elements shown in the figure.

At 2214 UTC, the first predicted tornado is at its strongest stage (*Fig. 13*a) and has been wrapped by cold air with two gust fronts located at southeast and northeast of the tornado along the boundary of warm and cold air. At 2217.5 UTC, the second tornado reaches its peak intensity and is located at the joint end of 'cold' and 'warm' gust fronts (*Fig. 13*b). Since then, the intensity of the second tornado is reduced but still maintains as a F2 until 2221 UTC. The predicted tornado at 2220 UTC has a lager core than its strongest stage and its connected gust fronts show the feature of occlusion (*Fig. 13*c). The predicted tornadoes share the same feathers during at the above three moments. They all have a circular-shaped area of strong surface vorticity that is circled by a strong ring-shaped circulation. In the center of the circulation, the wind is relatively weak but surface pressure deficit drop dramatically to maintain cyclostrophic balance. The winds right outside of the strongest circulation ring have a clear radial component into the circulation enter, and the surface friction must have played a role in enhancing the low-level convergence. All these features agree to the theoretical model of the wind, pressure, and temperature associated with a violent tornado.

The X-Z cross sections through the center of the tornado at the above three moments are also shown typical features of strong tornado (*Fig. 13*b, d, and f). The largest vertical vorticity of the column is near the surface, indicating the enhancement of circulation by the surface when the tornado outbreak. The low level of the center of the tornado is a weak downdraft wrapped by two updrafts above the strongest surface circulation ring. The updrafts are highly asymmetric, one is very strong and stretch to a high level while another one is much weaker and low.

In this study, the 50-m grid is used to capture more detailed structures of the tornado and its forecast has been analyzed in Xue and Hu (Xue and Hu 2007). Here the predicted tornado on the 50-m and 100-m grids are compared through repeating the same fields of *Fig. 13* in *Fig. 14* for the 20.5 min forecast of the 50-m grid, at which the predicted tornado on the 50-m forecast gives a well-defined vorticity ring with several maximum sub-vortex centers embedded. In the 100-m forecast, the strong vorticity center always covers the whole tornado core area and has a single maximum inside the tornado circulation (*Fig. 13*a, c, and e). In the core area of the predicted tornado, wind field on the 50-m grid shows a clear divergence pattern (*Fig. 14*a) which is also not found in the 100-m forecast. The vertical wind and vorticity structure of the predicted tornado on the 50-m and 100-m are similar (*Fig. 13*b, d, and f, *Fig. 14*b), but the updraft and downdraft associated to the tornado are stronger on the 50-m grid. Clearly, the finer grid gives more details of the tornado structures.

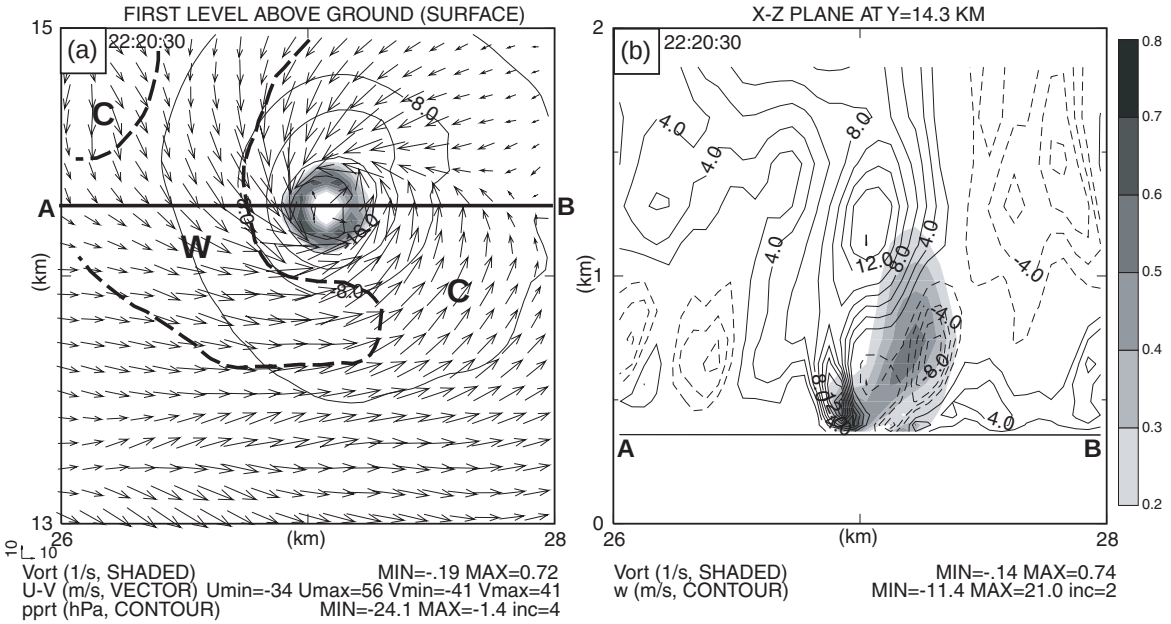

Fig. 14 (a) Same as Fig. 13a but for 20.5 min forecast of the 50-m grid and (b) same as Fig. 13b but for the cross-section along the line AB in (a). The dark dashed lines in (a) show the location of large temperature gradient. "W" and "C" indicate the area of warm and cold, respectively.

5. Summary

In this paper, high resolution experiments with 1-km, 100-m, and 50-m grid spacing are conducted to study the impact of assimilating radar data at a resolution similar to the radar observation density and the ability of the ARPS system in capturing the detailed structures of the 8 May 2003 Oklahoma City tornadic thunderstorm and even the OKC tornado itself. On the 1-km grid, rapid intermittent assimilations at 5-minute intervals, with a 70-minute assimilation window are used to generate the initial conditions for 2-h forecasts. The radial velocity data are analyzed by the ARPS 3DVAR and the reflectivity data through the ARPS cloud analysis procedure. The 100-m grid is one-way nested within the 1-km grid and its 1-h forecast starting from the initial condition interpolated from the 1-km grid assimilation results to capture the OKC tornado. To capture more details of the tornado, the 50-m grid is further one-way nested within the 100-m grid and start its 40-min forecast from the 20-min forecast of the 100-m grid to cover the entire OKC tornado outbreak.

Four 1-km experiments are conducted to study the impact of radar data on the storm forecast in a high resolution as compared to the earlier 3-km studies. By assimilating radial velocity and reflectivity data while imposing a 2D mass divergence constraint on the last two analyses, the 1-km control experiment successfully builds up a low-level cyclonic rotation center in its final analysis. The control experiment predicts the spinning up of the rotation center and the development of a hook-shaped echo at the southwestern end of the main Oklahoma City storm in the first 10 to 15 minutes of forecast. The forecast between 2210 and 2230 UTC (30 to 50 minutes of forecast) reproduces the development and propagation of the tornadic mesocyclone and associated hook-shaped echo with a displacement error of about 10 km only. Therefore, the 1-km control experiment captures great details of the Oklahoma City storm in its first 1-h of forecast.

The two 1-km experiments that use radial velocity data while impose the 2D mass divergence constraint on all analysis cycles or on none of the cycles, respectively, are also able to build up the low-level cyclonic rotation center in the assimilated fields and predict the spin-up of the rotation center in the first 10 to 20 minutes of forecast. However, the predicted mesocyclone and hook echo of the main storm during the period of the real tornado are much weaker and less well-defined than those in the control experiment.

Another experiment in which no radial velocity data are used fails to analyze and predict almost all the features associated with the low-level cyclonic rotation. Such large differences confirm the importance of assimilating radial velocity data for the definition of the low-level tornadic circulations that subsequently intensify in the model prediction. Comparing to our studies using a 3-km horizontal resolution, the impacts of the radar radial velocity are more evidence because the 1-km grid can better take advantage of the high-spatial resolutions of the radar data to resolve more detailed structures of storm.

The 1-km experiments also have some remaining problems. The most severe one is the formation of many small, spurious, cells in the forecast over 1 hour. The others include that the predicted cells propagate too fast and their path deviates from the observed one. These problems will be carefully investigated in the near future.

Despite some remaining problems with the 1-km forecast, the forecast of the main OKC storm is rather realistic, and it provides us with an excellent environment to further start extra-high resolution forecast to predict the tornado itself. In this study, two extra-high resolution forecasts on the 100-m and 50-m grid are conducted to predict the 8 May 2003 OKC tornado. Both forecasts successfully produce tornadoes of F1-F2 intensity with life span over 5 minutes during the period of the real tornado outbreak and traveling along a path within 8 km of the observed one.

The 100-m grid forecast is initiated a from a real initial condition at 2140 UTC, which has assimilated radar data in the past 70 minutes, and it produce the tornado starting at 2210 UTC. A half hour forecast leading time is achieved by the 100-m run for this tornado case. Also, the 100-m grid is large enough to capture the evolution of the entire tornado parent supercell during the forecast and the interaction between tornado and its parent storm should be correctly simulation either.

The analysis of the 50-m forecast in a previous paper indicates that the 50-m grid also successfully produces two F1-F2 intensity tornadoes. The comparing between the forecasts on the 100- and 50-m here found that the predicted tornado on the both grid travel along the similar path during the similar period. The similarity of the predicted tornado and the large predict domain confirms that tornado form as a result of dynamic adjustment of the wind field to the dynamics of the flow field.

In reality, a low-level mesocyclone within the tornado parent supercell was observed by the KTLX radar and been built into the initial field of the forecast by high frequency assimilation cycles on the 1-km grid with radar data. Apparently, this tornado parent mesocyclone plays a critical role in the successful prediction of tornadoes in the high-resolution forecast.

The above analysis clearly demonstrates that the OKC tornado been successfully predicted by the ARPS model starting from a real initial condition assimilating radar data. This tornado prediction is first ever of its kind and represents the significant improvements in ability of tornado study, which is greatly benefit from the rapid development of the nonhydrostatic model, supercomputer power, radar data assimilation. Although the predicted tornado is not lasting long enough and still has 8 km location error from the real OKC tornado, it is still very encouraging because it is generated in a realistic environment and can be used to further deeper our understanding of tornadogenesis and tornado dynamics, which is our research plan in the near future.

Acknowledgments

This work was supported by a DOT-FAA grant via DOC-NOAA NA17RJ1227. Xue was also supported by NSF grants ATM-0331756, ATM-0331594 and EEC-0313747. PSC high performance computing system was used for the experiments.

References

Bryan, G. H., J. C. Wyngaard, and J. M. Fritsch, 2003: Resolution Requirements for the Simulation of Deep Moist Convection. *Monthly Weather Review*, **131,** 2394-2416.

Gao, J.-D., M. Xue, K. Brewster, and K. K. Droegemeier, 2004: A three-dimensional variational data analysis method with recursive filter for Doppler radars. *J. Atmos. Ocean. Tech.*, **21,** 457-469.

Gao, J., M. Xue, K. Brewster, F. Carr, and K. K. Droegemeier, 2002: New development of a 3DVAR system for a nonhydrostatic NWP model. *Preprint, 15th Conf. Num. Wea. Pred. and 19th Conf. Wea. Anal. Forecasting*, San Antonio, TX, Amer. Meteor. Soc., 339-341.

Grasso, L. D. and W. R. Cotton, 1995: Numerical Simulation of a tornado vortex. *J. Atmos. Sci.*, **52,** 1192-1203.

Hu, M. and M. Xue, 2006: Impact of configurations of rapid intermittent assimilation of WSR-88D radar data for the 8 May 2003 Oklahoma City tornadic thunderstorm case. *Mon. Wea. Rev.***,** Accepted.

——, 2007: Impact of Configurations of Rapid Intermittent Assimilation of WSR-88D Radar Data for the 8 May 2003 Oklahoma City Tornadic Thunderstorm Case. *Monthly Weather Review*, **135,** 507-525.

Hu, M., M. Xue, and K. Brewster, 2006: 3DVAR and cloud analysis with WSR-88D level-II data for the prediction of Fort Worth tornadic thunderstorms. Part I: Cloud analysis and its impact. *Mon. Wea. Rev.*, **134,** 675-698.

Lewellen, D. C., W. S. Lewellen, and J. Xia, 2000: The Influence of a Local Swirl Ratio on Tornado Intensification near the Surface. *J. Atmos. Sci.*, **57,** 527-544.

Lewellen, W. S., 1993: Tornado vortex theory. The Tornado: Its Structure, Dynamics, Prediction and Hazards. *Geophys. Monogr.*, **No. 79,** Amer. Geophys. Union, 19-39.

Rotunno, R., 1984: An Investigation of a Three-Dimensional Asymmetric Vortex. *Journal of the Atmospheric Sciences*, **41,** 283-298.

Snyder, C. and F. Zhang, 2003: Assimilation of simulated Doppler radar observations with an ensemble Kalman filter. *Mon. Wea. Rev.*, **131,** 1663-1677.

Sun, J., 2005: Initialization and Numerical Forecasting of a Supercell Storm Observed during STEPS. *Monthly Weather Review*, **133,** 793-813.

Sun, J. and N. A. Crook, 1997: Dynamical and microphysical retrieval from Doppler radar observations using a cloud model and its adjoint. Part I: Model development and simulated data experiments. *J. Atmos. Sci.*, **54,** 1642-1661.

——, 1998: Dynamical and Microphysical Retrieval from Doppler Radar Observations Using a Cloud Model and Its Adjoint. Part II: Retrieval Experiments of an Observed Florida Convective Storm. *J. Atmos. Sci.*, **55,** 835-852.

Sun, J., D. W. Flicker, and D. K. Lilly, 1991: Recovery of three-dimensional wind and temperature fields from simulated single-Doppler radar data. *J. Atmos. Sci.*, **48,** 876-890.

Tong, M. and M. Xue, 2005: Ensemble Kalman filter assimilation of Doppler radar data with a compressible nonhydrostatic model: OSS Experiments. *Mon. Wea. Rev.*, **133,** 1789-1807.

Trapp, R. J., G. J. Stumpf, and K. L. Manross, 2005: A Reassessment of the Percentage of

Tornadic Mesocyclones. *Weather and Forecasting*, **20,** 680-687.

Wicker, L. J. and R. B. Wilhelmson, 1995: Simulation and analysis of tornado development and decay within a three-dimensional supercell thunderstorm. *J. Atmos. Sci.*, **52,** 2675-2703.

Wicker, L. J. and D. C. Dowell, 2004: High-resolution analyses of the 8 May 2003 Oklahoma City storm. Part III: An ultra-high resolution forecast experiment. *Preprints, 22nd Conf. Severe Local Storms,*, Hyannis, MA, Amer. Meteor. Soc., CDROM, 12.6.

Xue, M. and M. Hu, 2007: Prediction of 8 May 2003 Oklahoma City Tornado using high-resolution ARPS *Geophysical Research Letter*, **Submitted**.

Xue, M., K. K. Droegemeier, and V. Wong, 2000: The Advanced Regional Prediction System (ARPS) - A multiscale nonhydrostatic atmospheric simulation and prediction tool. Part I: Model dynamics and verification. *Meteor. Atmos. Physics*, **75,** 161-193.

Xue, M., M. Tong, and K. K. Droegemeier, 2006: An OSSE framework based on the ensemble square-root Kalman filter for evaluating impact of data from radar networks on thunderstorm analysis and forecast. *J. Atmos. Ocean Tech.*, **23,** 46–66.

Xue, M., K. K. Droegemeier, V. Wong, A. Shapiro, and K. Brewster, 1995: *ARPS Version 4.0 User's Guide*. [Available at http://www.caps.ou.edu/ARPS], 380 pp.

Xue, M., D.-H. Wang, J.-D. Gao, K. Brewster, and K. K. Droegemeier, 2003: The Advanced Regional Prediction System (ARPS), storm-scale numerical weather prediction and data assimilation. *Meteor. Atmos. Physics*, **82,** 139-170.

Xue, M., K. K. Droegemeier, V. Wong, A. Shapiro, K. Brewster, F. Carr, D. Weber, Y. Liu, and D. Wang, 2001: The Advanced Regional Prediction System (ARPS) - A multi-scale nonhydrostatic atmospheric simulation and prediction tool. Part II: Model physics and applications. *Meteor. Atmos. Phys.*, **76,** 143-166.

Zhang, F., C. Snyder, and J. Sun, 2004: Impacts of initial estimate and observations on the convective-scale data assimilation with an ensemble Kalman filter. *Mon. Wea. Rev.*, **132,** 1238-1253.

Zhang, J., 1999: Moisture and Diabatic Initialization Based on Radar and Satellite Observation, School of Meteorology, University of Oklahoma, 194.

Zhang, J., F. Carr, and K. Brewster, 1998: ADAS cloud analysis. *Preprints, 12th Conf. on Num. Wea. Pred.*, Phoenix, AZ., Amer. Met. Soc., 185-188.